Available online at www.sciencedirect.com

SciVerse ScienceDirect

Ceramics International 39 (2013) 4999–5005

CERAMICS INTERNATIONAL

www.elsevier.com/locate/ceramint

Kinetics of magnetite nanoparticles formation in a one step low temperature hydrothermal process

Reza Ahmadi[a,b,*], Afshin Masoudi[a], Hamid Reza Madaah Hosseini[a], Ning Gu[c]

[a]Department of Materials Science and Engineering, Sharif University of Technology, P.O. Box 11155-9466, Tehran, Iran
[b]Research Center for Molecular and Cellular Imaging (RCMCI), Tehran University of Medical Sciences, Tehran, Iran
[c]Jiangsu Key Laboratory of Biomaterials and Devices, Nanjing, China

Received 22 October 2012; received in revised form 17 November 2012; accepted 28 November 2012
Available online 23 December 2012

Abstract

In the present study, a one step hydrothermal process was employed to synthesize magnetite nanoparticles using oleic acid as surfactant agent at 140 °C. Effects of reaction time and alkalinity were studied on particles size and morphology. By changing these parameters, some monodisperse spherical nanoparticles with mean particle size between 2.71 and 13.88 nm were synthesized and characterized via TEM, XRD, VSM, TGA and FT-IR techniques. Assuming the Avrami behavior of particles formation, a kinetics equation was proposed for the transformation rate at 140 °C. Using some simplifying assumptions, nucleation and growth rates were calculated for the hydrothermal formation of magnetite nanoparticles at 140 °C.

Keywords: Magnetite; Hydrothermal; Avrami

1. Introduction

Transition metal oxide nanoparticles such as Fe_3O_4, MnO and Gd_2O_3 nanoparticles have been recently used in various biological applications such as drug delivery, MRI contrast agent and cancer therapy via hyperthermia [1–6]. Two important factors the high number of unpaired electrons and the long electron spin relaxation time of these transition metal ions, make their oxides suitable especially for MRI applications [7]. Among these materials, magnetite nanoparticles are more conventional due to their magnetic properties and excellent biocompatibility. In all of the above mentioned applications, one important parameter affecting particles uptake into a special tissue is particle size range. For example, regardless of other factors, magnetite nanoparticles with hydrodynamic size ranging between 20 and 40 nm mainly accumulate in lymph nodes, while large and aggregated ones (80–150 nm) are quickly absorbed in liver and spleen [1,2]. Among various procedures for synthesizing magnetite particles, thermal ones such as hydrothermal and thermal decomposition lead to formation of particles with narrow size distribution diagram. These procedures have been used by some researches through some multi-stage high temperature methods [8–10]. Among various parameters affecting particle size distribution, system alkalinity, temperature and reaction time play important roles. These parameters have been studied in various methods of magnetite nanoparticles synthesis [1,11]. Besides, kinetics of magnetite nanoparticles formation in the co-precipitation process has been recently investigated by this group [12].

Some diverse surfactants have been used to achieve particles stabilization in aqueous and non-aqueous media. These include PEG [13,14], dextran [1,15], PVP [16] and PVA [17] for aqueous and fatty acids such as oleic acid [11,18] for non-aqueous media. Using hydrothermal and thermal decomposition methods leads to formation of stable hydrocarbon-based ferrofluids of magnetite nanoparticles, but usually these ferrofluids are not directly applicable for biological applications and some supplementary surface exchange steps are required for particles transformation into aqueous medium [19,20].

*Corresponding author. Tel.: +98 91 2627 2374; fax: +98 21 6658 7530.
E-mail address: Reahmady@yahoo.com (R. Ahmadi).

0272-8842/$ - see front matter © 2012 Elsevier Ltd and Techna Group S.r.l. All rights reserved.
http://dx.doi.org/10.1016/j.ceramint.2012.11.097

In this study, a low temperature one-step hydrothermal process which has been recently introduced by this group [11] was modified through particles synthesizing at various alkalinity levels and reaction times using oleic acid as surfactant. Effect of these two parameters on particles size is discussed theoretically and particles formation kinetics was investigated using Thermogravimetric Analysis (TGA) and Transmission Electron Microscopy (TEM) results. Calculations are based on amount of oleic acid/particles ratio through reaction time interval. This approach might be useful for further investigations in which some exact amounts of particle size are required for a special application. Also, the synthesized particles were characterized using X-ray Diffraction (XRD), Fourier Transform Infrared Spectroscopy (FT-IR) and Vibrating Sample Magnetometry (VSM) techniques to investigate physical and chemical properties of synthesized particles.

2. Experimental

2.1. Sample preparation

All chemicals were of analytical grade and used as received without further purification. First, 0.6 M $FeSO_4 \cdot 7H_2O$ solution was provided via dissolving the salt in distilled water. Separately, the solution of 7 ml dimethyl sulfoxide (DMSO) and 3 ml oleic acid was prepared. These two solutions were mixed in a three neck container while argon was blown through the container for 10 min to reduce oxygen content of the solution. The argon purged container was put in a 140 °C oil bath while the iron source mixture was magnetically stirred. After that, 1.4 ml tetra methyl ammonium hydroxide (TMAH) 25% v/v was added to the flask as the reducing agent. Stirring was continued for 1 h and then the container was cooled down to room temperature. Through the hitting period, the mixture color gradually changed into light brown, dark brown and finally black. The black solid was removed from the mixture using magnetic and centrifugal separation. This product was washed three times with acetone and prepared for characterization tests (TEM, TGA, XRD, FT-IR and VSM). For evaluating effect of reaction time on particles' size, the above mentioned procedure was performed with reaction times of 5, 10, 30 and 120 min instead of 60 min. Besides, some samples were synthesized in the presence of 1 and 2 ml TMAH instead of 1.4 ml (Table 1).

2.2. Characterization methods

A Siemens D5000 X-ray theta/theta diffractometer was employed for XRD characterization using high-intensity Cu-K_α radiation ($\lambda = 1.5406$ Å) via movement of both the X-ray source and detector. The XRD scan rate was fixed at $0.02^\circ\ s^{-1}$ and the step size was 0.02°. IR spectra were recorded on a Nicolet spectrometer (Magna 500). Powder samples were dried at 70 °C before fabrication of KBr pellet. A JEOL TEM JEM-2010F was used to determine the average particle size and morphology of the powders on an accelerating voltage of 200 kV. Sample preparation was performed through the conventional method in which one trickle of ferrofluid is located on the surface of a carbon coated copper grid and used as TEM sample after trickle drying. A Lakeshore 7470 VSM instrument was used for magnetometry. Solid samples were used for determination of solid samples' magnetization curve. TGA was performed using a TGA Q50 instrument in order to investigate specimen weight changes.

3. Results and discussion

3.1. TEM

TEM images of samples A1–A5 synthesized at 5, 10, 30, 60 and 120 min are presented in Fig. 1a–e, in order. These samples were synthesized at 140 °C in the presence of 1.4 ml TMAH. Size distribution histograms of these samples obtained via considering at least 50 particles are attached into TEM images. According to these diagrams, mean particle size of samples A1–A5 varies from 2.71 nm to 6.83 nm, (Table 1). Particles are semi-spherical in shape and monodispersed without considerable agglomeration. Electron beam diffraction pattern and HRTEM image of sample A4 are shown in Fig. 2, revealing inverse spinel structure of this sample. The interplanar distance calculated from Fig. 2b well matches with that of (400) planes in pure magnetite.

TEM image of samples B1 and B2, synthesized in the presence of 1 and 2 ml TMAH is illustrated in Fig. 3. Comparing with sample A4 synthesized in similar conditions with 1.4 ml TMAH, mean particle size is increased with decreasing amount of TMAH. This could be explained as follows: decreasing amount of TMAH leads to decreasing

Table 1
Experimental conditions of synthesizing samples in this research. Oil bath temperature was 140 °C in all experiments.

Sample	Reaction time (min)	Amount of TMAH (ml)	d_{TEM} (nm)	M_s (emu/g)
A1	5	1.4	2.71	16.84
A2	10	1.4	3.73	20.37
A3	30	1.4	5.6	42.53
A4	60	1.4	6.34	60.71
A5	120	1.4	6.83	64.11
B1	60	1	13.88	
B2	60	2	4.13	

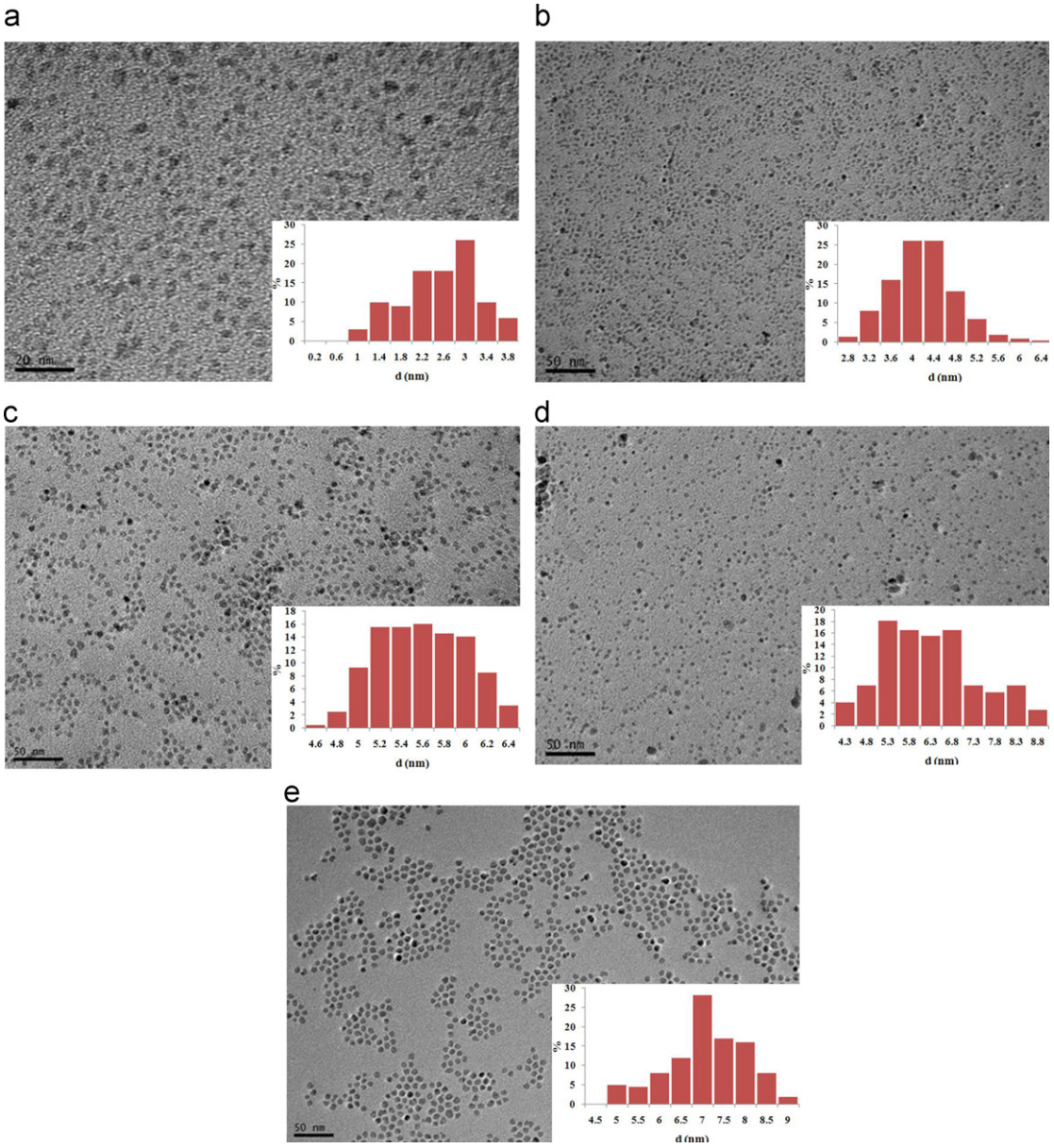

Fig. 1. TEM images of samples A1–A5 with mean particle size of (a) A1: 2.71 nm, (b) A2: 3.73 nm, (c) A3: 5.6 nm, (d) A4: 6.34 nm and (e) A5: 6.83 nm (Table 1). These data were obtained via measuring at least 100 particles.

particles' negative surface charge due to decreasing amount of OH^- anions. So, particles mean diameter is increased though an aggregation mechanism. This decrement in amount of electrostatic repulsion has been thought to be the main reason for magnetite nanoparticles growth rate enhancement in the co-precipitation process too [1].

3.2. VSM

VSM diagrams of samples A1–A5 are presented in Fig. 4. All of these samples show superparamagnetic behavior with saturation magnetizations between 16.84 and 64.11 emu/g and very low coercivities, near zero (Table 1). This is in good coincidence with TEM results and the fact that superparamagnetic size of Fe_3O_4 nanoparticle is larger than 6.83 nm. Samples' saturation magnetization is increased with particle size. This is mainly due to the so-called "magnetically dead" region in nanoparticles' surface area in which magnetic order is not completely satisfied [21].

3.3. XRD

XRD pattern of sample A4 is shown in Fig. 5, exposing inverse spinel structure of the synthesizing nanoparticles. The indicated peaks are well matched with those of pure magnetite (JCPDS card no. 19-0629). The chemical mechanism of magnetite particles formation can be briefly described as follows: DMSO acts as the oxidizing agent for conversion of Fe^{2+} to Fe^{3+}. After this conversion,

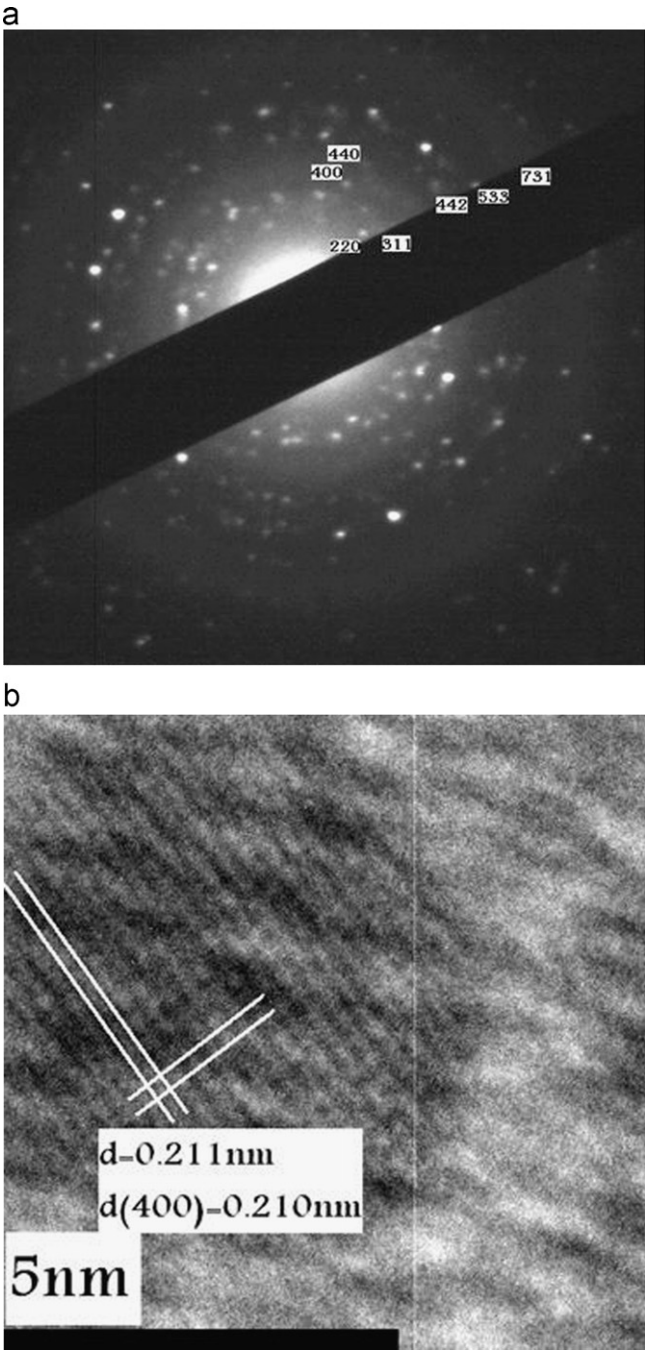

Fig. 2. (a) Electron beam diffraction pattern of sample A4 revealing reverse spinel structure of synthesized particles, and (b) HRTEM image of sample A4 revealing lattice fringes (400) of magnetite.

Fe_3O_4 nanoparticles form in the presence of OH^- accordingly:

$$Fe^{2+} + 2Fe^{3+} + 8OH^- \rightarrow Fe_3O_4 + 4H_2O \quad (1)$$

The source of OH^- is TMAH.

Crystallite size of magnetite nanoparticles can be calculated from XRD pattern using the Scherrer equation:

$$d = \frac{0.9\lambda}{\beta \cos\theta} \quad (2)$$

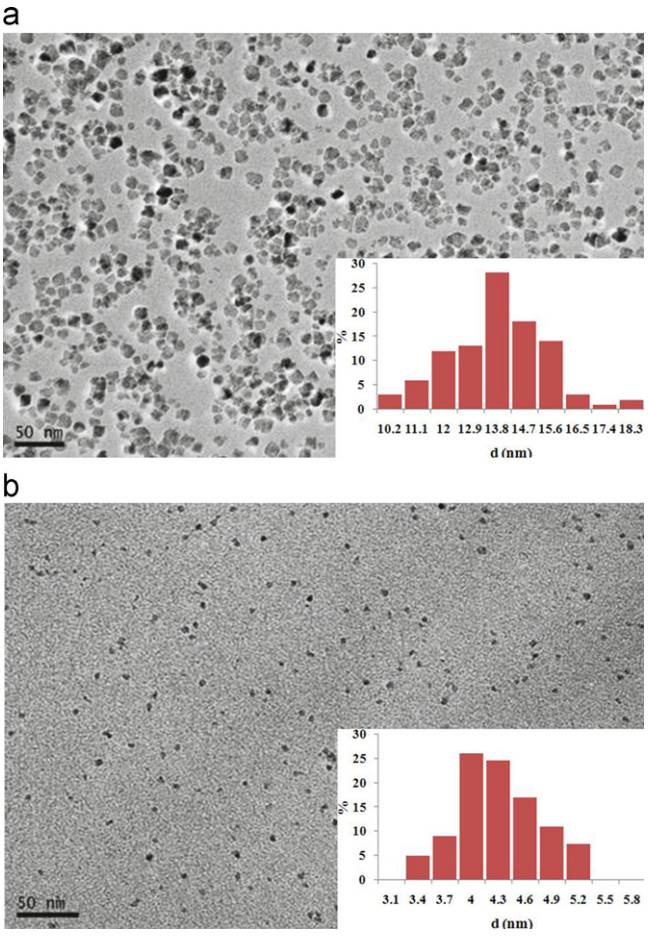

Fig. 3. TEM image of samples B1 and B2 with mean particle size of (a) B1: 13.88 nm and (b) B2: 4.13 nm in comparison with sample A4 (Table 1 and Fig. 1d).

where d is the crystallite size, λ is the X-ray wavelength, and β is the full width at half maximum (FWHM) of the peak located at the Bragg angle (2θ). Using $\lambda = 1.5406$ Å, $\beta = 1.38^{\circ} = 0.024^{\text{rad}}$ and $2\theta = 35.5^{\circ}$, the average crystallite size of magnetite nanoparticles is about 6.04 nm which is in good concurrence with the TEM result (6.34 nm).

3.4. FT-IR

Fig. 6 presents the FT-IR spectra of sample A4. The sharp peak at 582 cm^{-1} belongs to the stretching mode of Fe–O in Fe_3O_4 [22]. The two peaks at 1425 and 1558 cm^{-1} are related to the symmetric and asymmetric stretching modes of COO^- group respectively. Also, the peaks seen at 2848 and 2917 cm^{-1} could be attributed to the symmetric and asymmetric stretching modes of C–H bond, respectively. Finally, the wide band in the 3200–3600 cm^{-1} range is related to the O–H vibration. These peaks verify the presence of oleic acid molecules on the surface of magnetite nanoparticles.

3.5. TGA

Fig. 7 illustrates TGA curves of samples A1–A5, revealing a decrease in amount of weight loss with increasing reaction

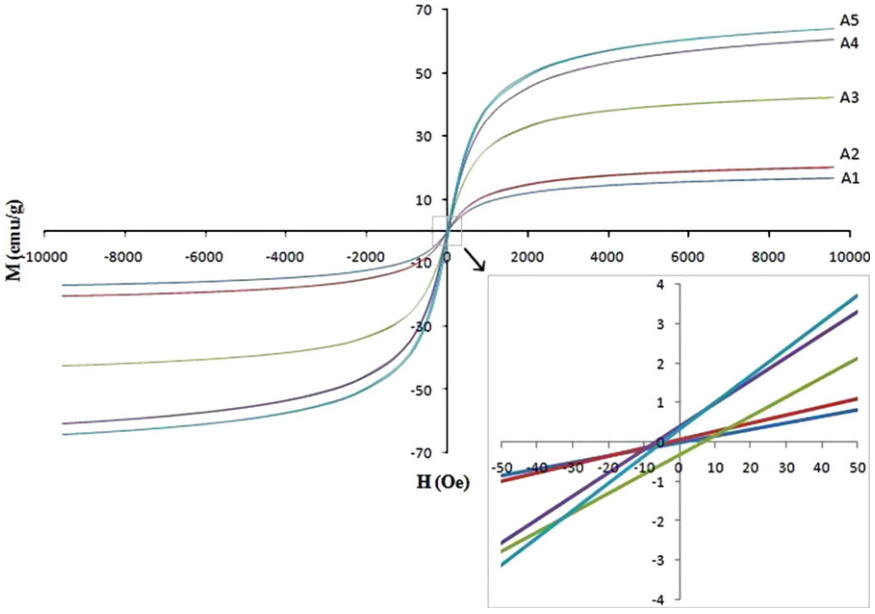

Fig. 4. VSM diagrams of the synthesized samples with saturation magnetizations of 16.84, 20.37, 42.53, 60.71 and 64.11 emu/g for samples A1, A2, A3, A4 and A5, respectively (Table 1).

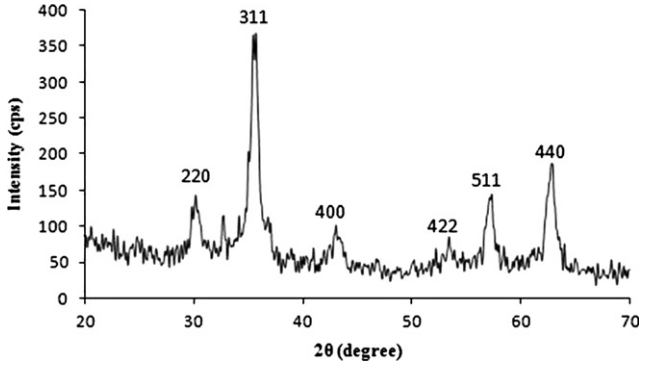

Fig. 5. XRD pattern of sample A4.

time. As the total amount of oleic acid is constant and equal in the synthesis process of samples A1–A5, this change in amount of weight loss is related to variation in amount of magnetite nanoparticles forming in the reaction time interval. Kinetics of particles formation could be studied using the method that has been previously used by this group [12]. Supposing the Avrami behavior of particles formation, rate of transformation can be described as [23]

$$f(t) = 1 - \exp(-kt^n) \quad (3)$$

where $f(t)$ is fraction progress of reaction, t is time and k and n are kinetics coefficients. Eq. (3) can be written as

$$\ln[-\ln(1-f(t))] = \ln k + n \ln t \quad (4)$$

In other words, if the plot $\ln[-\ln(1-f(t))]$ versus $\ln t$ reveals a linear or semi-linear behavior, the rate of particles formation has an Avrami behavior. In these conditions, n and $\ln k$ can be considered as the line slope and intercept with vertical axis, respectively. So, the kinetics equation of particles formation can be written according to Eq. (1).

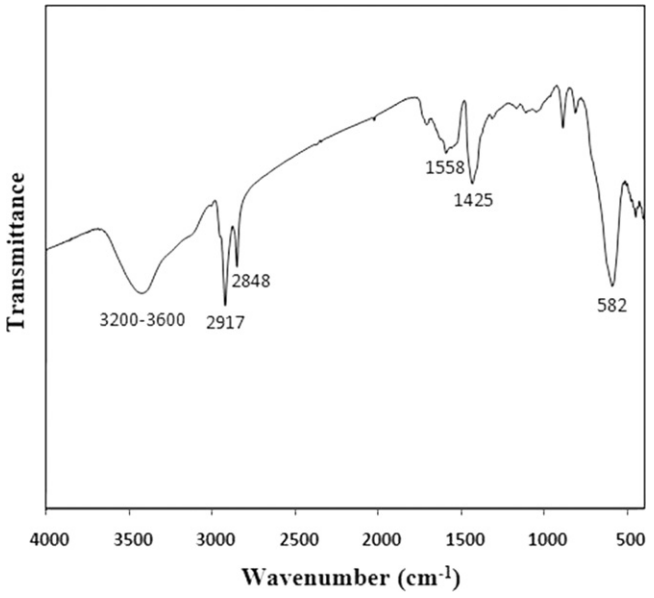

Fig. 6. FT-IR spectra of sample A4.

As $f(t)$ can be calculated using TGA results, the above mentioned equation can be obtained accordingly: the fraction of weight loss of samples A1, A2, A3, A4 and A5 synthesized at 140 °C after 5, 10, 30, 60 and 120 min are 84.82%, 72.79%, 36.59%, 18.66% and 15.3%, respectively. These amounts are related to severe weight losses which began at about 360 °C, the oleic acid boiling point (Fig. 7). So, the fraction of magnetite is 15.18%, 27.21%, 63.41%, 81.34% and 84.70% for samples A1–A5, in order. Diagram of weight loss fraction versus hydrothermal reaction time is plotted in Fig. 8a. Assuming that the change in the amount of weight loss is negligible after

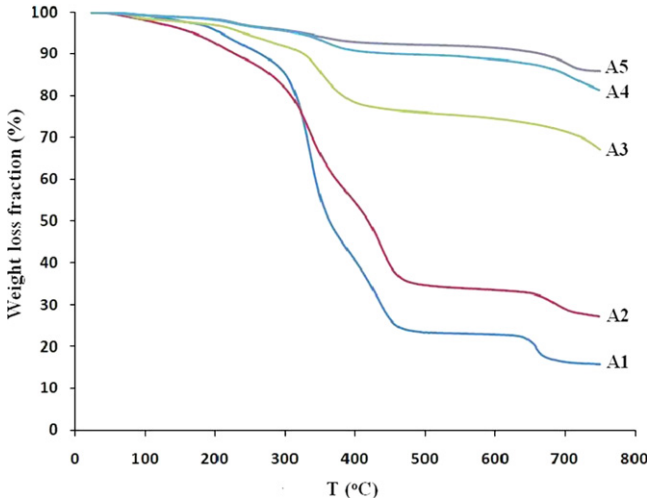

Fig. 7. TGA diagrams of samples A1–A5.

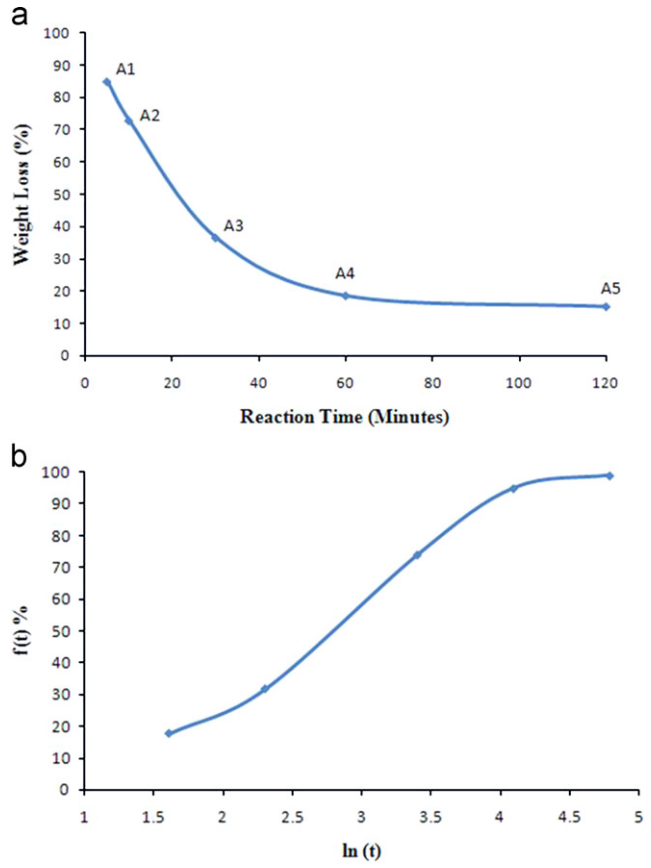

Fig. 8. (a) Diagram of weight loss of synthesized sample at various reaction times from TGA results and (b) diagram of transformation progress versus reaction time.

120 min, this time can be considered as $t_{0.99}$, the time in which 99% of reaction is completed. This is in good coincidence with the fact that curve slope tends to zero at this time (Fig. 8a). So, the fraction progress of reaction $f(t)$can be considered as 17.73%, 31.78%, 74.05%, 94.99% and 99% for samples A1–A5, in order (Fig. 8b). The "S" shape type curve seen in this figure is similar to those with the Avrami behavior. To investigate this behavior, the diagram $\ln[-\ln(1-f(t))]$ versus $\ln t$ was plotted according to the above mentioned amounts of $f(t)$. This plot is presented in Fig. 9. As seen in this figure, the curve could be trended with accepted linearity in the whole range of reaction time. As discussed above, this is the sign of particles' formation through the Avrami kinetics model in which transformation rate is slow in the start and end of the reaction, while it has its maximum value in intermediate times (Fig. 8b). So, n and k could be calculated from the trend line slope and intercept with vertical axis, respectively. According to Fig. 9, $k=0.0375$ and $n=1.0338$. As n is near 1, the nucleation growth is constant through the reaction [23]. Using this approach, the kinetics equation of particles formation in this hydrothermal process at 140 °C (413 K) could be considered as

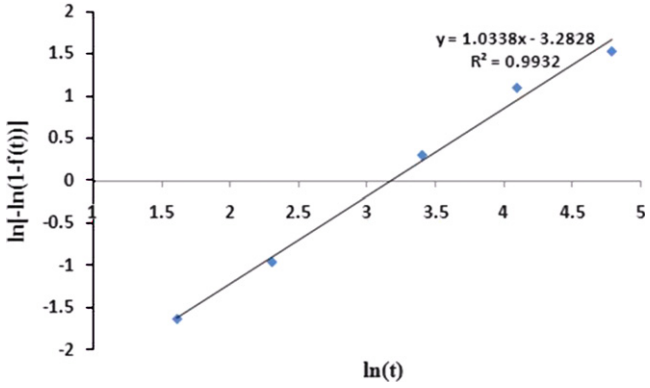

Fig. 9. Diagram of $\ln[-\ln(1-f(t))]$ versus $\ln t$ at 140 °C.

$$f_{413}(t) = 1-\exp(-0.0375t^{1.0338}) \quad (5)$$

In the spherical growth of particles, k is defined by assuming some simplifying assumptions [23]:

$$k = \tfrac{4}{3}\pi N v^3 \quad (6)$$

According to the TEM results, especially Fig. 3e the nanoparticles' average growth rate $v = 6.83\ \text{nm}/120\ \text{min} = 0.0569\ \text{nm/min}$. So, considering semi-spherical particles growth, the number of nucleation points N is 4.86×10^{28} nuclei/m^3 which is a reliable amount for homogeneous nucleation of initial nucleus.

4. Conclusion

In this study, some monodispersed spherical magnetite nanoparticles were synthesized via a one step low temperature hydrothermal process. Particles mean size was enhanced by increasing reaction time and decreasing system alkalinity accordingly: particles mean size was increased from 2.71 to 6.83 nm by increasing reaction time from 5 to 120 min. Also, particles mean size was increased from 4.13 to 13.88 nm by decreasing amount of TMAH as the alkaline reducing agent from 2 to 1 ml. The kinetics equation of particles formation was determined as $f_{413}(t) = 1-\exp(-0.0375t^{1.0338})$, revealing

the Avrami behavior of particles formation with the constant rate of nucleation. The number of nucleation points and particles growth rate for this process were determined as 4.86×10^{28} nuclei/m^3 and 0.0569 nm/min, respectively.

References

[1] R. Ahmadi, M. Malek, H.R. Madaah Hosseini, M.A. Shokrgozar, M.A. Oghabian, A. Masoudi, N. Gu, Z. Yu, Ultrasonic-assisted synthesis of magnetite based MRI contrast agent using cysteine as the biocapping coating, Materials Chemistry and Physics 131 (2011) 170–177.

[2] R. Ahmadi, N. Gu, H.R. Madaah Hosseini, Characterization of cysteine coated magnetite nanoparticles as MRI contrast agent, Nano–Micro Letters 4 (3) (2012) 180–183.

[3] M.M. Rashad, H.M. El-Sayed, M. Rasly, M.I. Nasr, Induction heating studies of magnetite nanospheres synthesized at room temperature for magnetic hyperthermia, Journal of Magnetism and Magnetic Materials 324 (2012) 4019–4023.

[4] Z. Zipeng, X. Jin, Development of manganese-based nanoparticles as contrast probes for magnetic resonance imaging, Theranostics 2 (2012) 45–54.

[5] M.J. Baek, J.Y. Park, W. Xu, K. Kattel, H.G. Kim, E.J. Lee, Water-soluble MnO nanocolloid for a molecular T_1 MR imaging: a facile one-pot synthesis, in vivo T_1 MR images and account for relaxivities, ACS Applied Materials and Interfaces 2 (2010) 2949–2955.

[6] M. Ahrén, L. Selegård, A. Klasson, F. Söderlind, N. Abrikossova, C. Skoglund, Synthesis and characterization of PEGylated Gd_2O_3 nanoparticles for MRI contrast enhancement, Langmuir 26 (2010) 5753–5762.

[7] R.E. Hendrick, E.M. Haacke, Basic physics of MR contrast agents and maximization of image contrast, Journal of Magnetic Resonance Imaging 3 (1993) 137–148.

[8] T.J. Daou, G. Pourroy, S. Bégin-Colin, J.M. Grenèche, C. Ulhaq-Bouillet, P. Legaré, Hydrothermal synthesis of monodisperse magnetite nanoparticles, Chemistry of Materials 18 (2006) 4399–4404.

[9] W.W. Yu, J.C. Falkner, C.T. Yavuz, V.L. Colvin, Synthesis of monodisperse iron oxide nanocrystals by thermal decomposition of iron carboxylate salts, Chemical Communications 10 (2004) 2306–2307.

[10] A.G. Roca, M.P. Morales, K. O'Grady, C.J. Serna, Structural and magnetic properties of uniform magnetite nanoparticles prepared by high temperature decomposition of organic precursors, Nanotechnology 17 (2006) 2783–2788.

[11] C.Y. Wang, J.M. Hong, G. Chen, Y. Zhang, N. Gu, Facile method to synthesize oleic acid-capped magnetite nanoparticles, Chinese Chemical Letters 21 (2010) 179–182.

[12] R. Ahmadi, H.R. Madaah Hosseini, A. Masoudi, Avrami behavior of magnetite nanoparticles formation in co-precipitation process, Journal of Mining and Metallurgy, Section B: Metallurgy 47 (2) (2011) 211–218.

[13] Y. Zhang, N. Kohler, M. Zhang, Surface modification of superparamagnetic magnetite nanoparticles and their intracellular uptake, Biomaterials 23 (2002) 1553–1561.

[14] A. Masoudi, H.R. Madaah Hosseini, M.A. Shokrgozar, R. Ahmadi, M.A. Oghabian, The effect of poly(ethylene glycol) coating on colloidal stability of superparamagnetic iron oxide nanoparticles as potential MRI contrast agent, International Journal of Pharmaceutics 433 (2012) 129–141.

[15] J. Ding, K. Tao, J. Li, S. Song, K. Sun, Cell-specific cytotoxicity of dextran-stabilized magnetite nanoparticles, Colloids and Surfaces B: Biointerfaces 79 (2010) 184–190.

[16] H. Liu, P. Hou, W. Zhang, J. Wu, Synthesis of monosized core–shell Fe_3O_4/Au multifunctional nanoparticles by PVP-assisted nano-emulsion process, Colloids and Surfaces A: Physicochemical and Engineering Aspects 356 (2010) 21–27.

[17] J. Lee, T. Isobe, M. Senna, Preparation of ultrafine Fe_3O_4 particles by precipitation in the presence of PVA at high pH, Journal of Colloid and Interface Science 177 (1996) 490–494.

[18] L. Zhang, R. He, H.C. Gu, Oleic acid coating on the monodisperse magnetite nanoparticles, Applied Surface Science 253 (2006) 2611–2617.

[19] Y. Wu, C. Wang, L. Wu, T. Yang, X. Zhang, Y. Zhang. Proceedings of the Seventh China–Korea Symposium on Biomaterials and Nano-Biotechnology, Nanjing/Suzhou, China, October 19–23 2009.

[20] Z.P. Chen, Y. Zhang, S. Zhang, J.G. Xia, J.W. Liu, K. Xu, N. Gu, Preparation and characterization of water-soluble monodisperse magnetic iron oxide nanoparticles via surface double-exchange with DMSA, Colloids and Surfaces A: Physicochemical and Engineering Aspects 316 (2008) 210–216.

[21] M. Všianská, M. Sob, Magnetically dead layers at sp-impurity-decorated grain boundaries and surfaces in nickel, Physical Review B 84 (2011) art. no. 014418.

[22] R.Y. Hong, T.T. Pan, H.Z. Li, Microwave synthesis of magnetic Fe_3O_4 nanoparticles used as a precursor of nanocomposites and ferrofluids, Journal of Magnetism and Magnetic Materials 303 (2006) 60–68.

[23] D.A. Porter, K.E. Easterling, Phase Transformations in Metals and Alloys, CRC Press, 1992.